



# Modelling the thermal evolution of slow-spreading ridge segments and their off-axis geophysical signature

Sébastien Gac, Chantal Tisseau, Jérôme Dymont, Jean Goslin

## ► To cite this version:

Sébastien Gac, Chantal Tisseau, Jérôme Dymont, Jean Goslin. Modelling the thermal evolution of slow-spreading ridge segments and their off-axis geophysical signature. *Geophysical Journal International*, Oxford University Press (OUP), 2005, 164 (2), pp.341-358. <10.1111/j.1365-246X.2005.02844.x>. <insu-01352918>

**HAL Id: insu-01352918**

**<https://hal-insu.archives-ouvertes.fr/insu-01352918>**

Submitted on 10 Aug 2016

**HAL** is a multi-disciplinary open access archive for the deposit and dissemination of scientific research documents, whether they are published or not. The documents may come from teaching and research institutions in France or abroad, or from public or private research centers.

L'archive ouverte pluridisciplinaire **HAL**, est destinée au dépôt et à la diffusion de documents scientifiques de niveau recherche, publiés ou non, émanant des établissements d'enseignement et de recherche français ou étrangers, des laboratoires publics ou privés.

# Modelling the thermal evolution of slow-spreading ridge segments and their off-axis geophysical signature

Sébastien Gac,<sup>1,3</sup> Chantal Tisseau,<sup>1</sup> Jérôme Dymont<sup>2,\*</sup> and Jean Goslin<sup>1</sup>

<sup>1</sup>CNRS UMR 6538 Domaines Océaniques, Institut Universitaire Européen de la Mer, Université de Bretagne Occidentale, Brest, France.

E-mail: chantal.tisseau@univ-brest.fr

<sup>2</sup>Equipe de Géosciences Marines, CNRS UMR 7154 Institut de Physique du Globe, Paris, France

<sup>3</sup>Department of Earth Science, The University of Bergen, Bergen, Norway

Accepted 2005 October 10. Received 2005 July 22; in original form 2004 September 24

## SUMMARY

Systematic studies conducted between 15°N and 40°N over ridge segments along the slow-spreading Mid-Atlantic Ridge (MAR) have shown that segment characteristics are related to the thermal state of the segments and gradually vary with their length. This paper presents further developments of a 3-D model, based on the presence of a hot zone located under the segment centres (Gac *et al.* 2003), to (1) quantify the thermal structures and the geophysical signatures of segments of various lengths, considered as representative of the various MAR segments; (2) test if a simple and single model of thermal evolution can account for the characteristics of all segments and (3) explain the past evolution of the segmentation, as is observed off-axis along the MAR.

The modelled thermal structure and three simulated geophysical outputs [crustal structure, along-axis variations of the earthquake maximum depth and the mantle Bouguer gravity anomalies (MBA)] are found to be directly controlled by the shape (geometry and dimensions) of the hot zone. A consistent fit between model outputs and along-axis variations of the geophysical observables over the various segments is obtained by varying solely the length of the hot zone. This result shows that segments of different length may in fact constitute the different stages of a single evolution process: the axial geophysical characteristics of the segment would progressively evolve from those of shorter segments to those of longer ones, as the hot zone lengthens along-axis. A subsequent shortening of the segment would result from a simultaneous shortening of the hot zone, segment characteristics reverting back from those of longer segments to those of shorter ones.

Three geophysical fields (topography, gravity and magnetic anomalies) are simulated as the results of the thermal evolution of aligned and offset segments the length of which evolves through time. These simulations succeed in fitting observations for the entire range of observed axis offsets between adjacent MAR segments. The segment evolution produces peculiar off-axis isostatic topography and gravity anomaly (MBA), the rhomb-shaped patterns. Our simulations, which model adjacent offset segments having evolved through several cycles of lengthening and shortening, yield a good fit to the isostatic topography and MBA patterns observed in the off-axis region. Finally, the distribution of magnetization depends on the magnetic properties of each type of rocks and on the petrological structure of the lithosphere, which, in turn, results from its thermal structure and evolution. Modelled magnetic anomalies are shown to be in good agreement with off-axis observations along the N21°40' segment (TAMMAR) of the MAR.

**Key words:** accretion processes, mid-oceanic ridges, thermal modelling.

## 1 INTRODUCTION: VARIABILITY OF SEGMENT CHARACTERISTICS AND THERMAL STRUCTURE

Slow-spreading ridges, such as the Mid-Atlantic Ridge (MAR), are characterized by a short-wavelength axial segmentation, the segment

\*Formerly at: CNRS UMR 6538 Domaines Océaniques, Institut Universitaire Européen de la Mer, Université de Bretagne Occidentale, Brest, France.

lengths being typically less than 100 km (Le Douaran & Francheteau 1981; Macdonald *et al.* 1984, 1986; Sempéré *et al.* 1990, 1993). This segmentation has been characterized by the variability of several parameters along each ridge segment. Morphological variations of the axial valley are systematically observed: the segment centre is always associated with a shallow and narrow axial valley, which widens and deepens towards the segment ends (Crane & Ballard 1981; Sempéré *et al.* 1990; Durand *et al.* 1995). These variations in the morphology are accompanied by an increase of the absolute value of the difference of mantle Bouguer anomaly (MBA) between segment centres and segment ends (hereafter called the  $\Delta$ MBA). Along-ridge, the MBA ‘bull’s eye’ anomalies reveal variations in the crustal thickness and/or variations in the mantle and/or crustal densities, due to focused upwelling (or diapir) of hot mantle material beneath the segment centres (Kuo & Forsyth 1988; Lin *et al.* 1990). Discussing the origin of such an upwelling is outside the scope of this paper, and we have chosen to invoke the presence of a hot zone without any *a priori* inference on its emplacement mechanism and dynamics.

The presence of such a hot zone is supported by other geophysical observations. Microseismicity studies show that the maximum depth of earthquakes increases from segment centres to segment ends (Kong *et al.* 1992; Barclay *et al.* 1993; Toomey *et al.* 1993; Wolfe *et al.* 1995), thus reflecting a deepening of the brittle–ductile transition, often attributed to the comparable deepening of an isotherm towards the segment ends. Seismic refraction experiments (Tolstoy *et al.* 1993; Hooft *et al.* 2000; Canales *et al.* 2000) show that the crust, produced by the melting of upper mantle material, thins towards segment ends. This result is consistent with the frequent outcropping of mantle rocks near segment ends (Juteau *et al.* 1990; Cannat 1993; Cannat *et al.* 1995).

Slow-spreading ridges are also characterized by a strong variability of the above-mentioned parameters between different segments. In fact, segments present a more or less pronounced contrast between their centre and ends. Shallower and narrower is the axial valley at the segment centre, higher is the  $\Delta$ MBA and, therefore, thicker may be the crust beneath the centre. A deep and wide valley along most of the segment goes with a low-amplitude  $\Delta$ MBA and a nearly uniform crustal thickness. This variability among segments has been interpreted as resulting from the thermal characteristics of a hot zone beneath the segment centre. Adjacent segments may be considered as being in different thermal states, as coined by the terms ‘hot’ or ‘cold’ segment, often used in the literature.

Moreover systematic studies conducted along MAR segments between 15°N and 40°N (Detrick *et al.* 1995; Thibaud *et al.* 1998) show that segment characteristics gradually vary with the length of the segment. In particular, the  $\Delta$ MBA increases and the axial valley becomes progressively shallower and narrower at segment centres, as the segment length increases. These variations would result from change in the thermal structure of the segment which, in turn, would be directly related to its length. The shortest segments would thus be ‘colder’, the longest segments would be ‘hotter’.

Finally, off-axis surveys carried out along several sections of the MAR clearly show that the length of a given segment may vary through time. For example, south of the Kane Fracture Zone, clear rhomb-shaped areas are observed over 0–10-Myr-old crust in the SEADMA zone (Gente *et al.* 1994, 1995). These areas are limited by oblique structures, neither parallel to the ridge axis nor to the direction of spreading, past traces of the axial discontinuities (called below ‘oblique discontinuities’). Some segments have lengthened at the expense of their neighbours and have subsequently

shortened during periods lasting 3–6 Myr. Thus, considering that segment length and thermal state are linked, the description and parameterization of lengthening and shortening cycles surely represent an important constraint to model the thermal evolution of segments.

Gac *et al.* (2003) have presented in a previous paper the conceptual details of the 3-D thermal simulation of a slow-spreading ridge segment, and used this simulation scheme to model along-axis geophysical observables (MBA, depths of earthquake foci and crustal thickness) along a typical 50-km-long ridge segment. The modelling was achieved by supposing the *a priori* existence of a permanent hot zone under the centre of each segment. The shape of this hot zone (geometry and dimensions) was adjusted in order to fit model outputs to the observations.

The present paper increases the capabilities of the modelling scheme to a large extent. Our general approach is summarized in Fig. 1: first, individual segments of various length are modelled in Section 2 (sketch in Fig. 1, top); second, possible synchronous variations of the length of adjacent segments are taken into account (Section 3) and, finally, off-axis observations are modelled, taking into account variable offsets at inter-segment discontinuities. This will allow, in Section 4, some insight on the off-axis past evolution of slow-spreading ridge segments (sketch in Fig. 1, bottom).

## 2 THERMAL STRUCTURE BENEATH SLOW-SPREADING RIDGE SEGMENTS

In this section, we model steady-state segments with three different lengths, considered as representative samples of the various segments observed along a slow-spreading ridge such as the MAR: a short (30 km), a medium (50 km) and a long (90 km) segment. As stated above, these are often viewed as a cold, a warm and a hot segments, respectively. For each segment length, we will model the ‘best’ thermal structure beneath the segment, that is, the one which better accounts for its geophysical signature.

### Modelling the thermal structure and geophysical outputs: concept

The thermal structure is modelled as resulting from the presence of a hot zone, assumed *a priori*, beneath the segment centre. This hot zone is a region where the temperature is imposed and kept constant through time, in order to simulate the upwelling of mantle material. In this section, the hot zone is considered as permanent. Outside the hot zone, the temperature is computed using the heat equation. Heat transfer takes place by conduction in the three directions, by advection due to the horizontal-spreading plate motion, and by heat loss due to melting (Tisseau & Tonnerre 1995). Three geophysical outputs, which depend highly on temperature are simulated from the thermal structure and fitted to observations to constrain the parameters of the model. These outputs are:

- (1) the  $\Delta$ MBA,
- (2) the crustal thickness variation along the segment and
- (3) the maximum depth of earthquake foci at segment centres and segment ends.

The MBA is computed from density variations, which diversely depend on the thermal structure: the thermal volume expansion, the presence of liquid in the melting zone, the density contrast between the crust (2800 kg m<sup>-3</sup> at 0°C) and the mantle (3300 kg m<sup>-3</sup> at 0°C) and the density variation of peridotites due to serpentinization

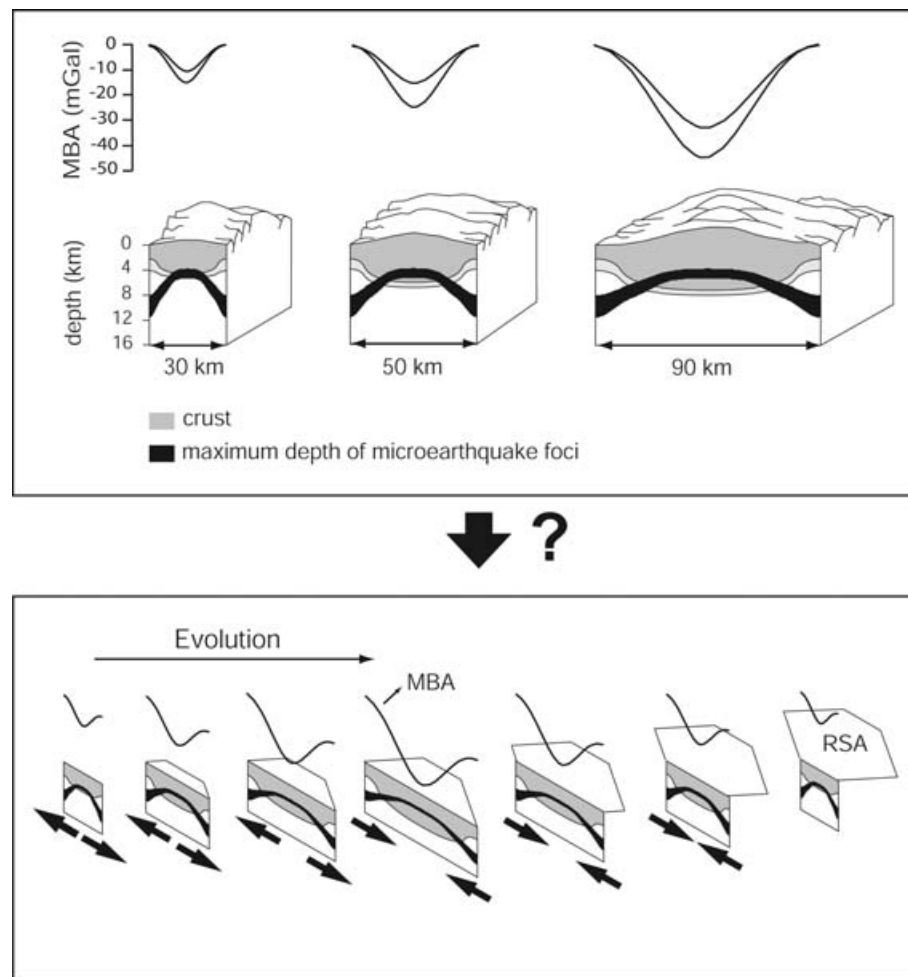


**Figure 1.** Conceptual sketches illustrating the approach adopted in this study. The upper part summarizes the geophysical features explained with the modelled thermal structure beneath the three sample segments considered as representative of the various MAR segments (Section 2 in the text). The schematic morphology is also shown. The lower part illustrates the hypothesis of a single type of segment, which evolution accounts for the axial geophysical characters (Section 3 in the text) and explains the off-axis geophysical signature and its peculiar rhomb-shaped patterns (Section 4 in the text).

(Christensen 1966). The crustal thickness is calculated directly from the volume of liquid in the partial melting zone which is controlled by the temperature distribution. Only a fraction of the extracted liquid is considered reaching the surface; this fraction is adjusted to produce a 6-km-thick crust (average thickness of the normal oceanic crust) at the centre of 50-km-long segment (Gac *et al.* 2003). Finally, the maximum depth of earthquakes marks the brittle/ductile transition; it corresponds to the depth of the 750°C isotherm for peridotite and to the depth of the 500°C isotherm for the oceanic crust (Chen & Molnar 1983). Details of the modelling of these model outputs are given in Gac *et al.* (2003).

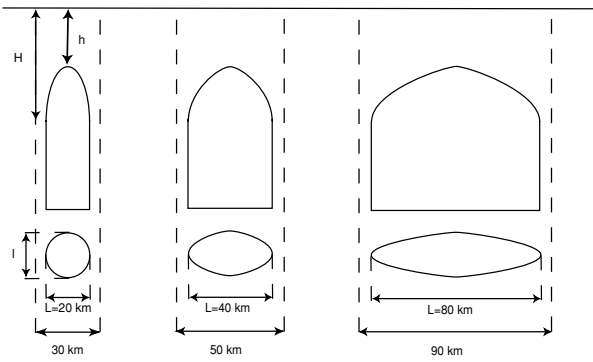
The thermal structure, and therefore the three resulting modelled geophysical outputs, is found to be directly controlled by the shape (geometry and dimensions) of the hot zone. For each segment length, the optimal shape of the hot zone is determined by comparing the model outputs with the observations for different shapes of the hot zone. This comparison is iterated till the shape producing the best fit between modelled and observed geophysical parameters is reached. So, modelling the thermal structure of a segment of fixed given length first amounts to a search for the ‘best-fitting shape’ of the hot zone.

### The ‘best-fitting shape’ of hot zones beneath the segments

As was done in our previous study (Gac *et al.* 2003), we have tested two end-members’ geometries for the hot zone beneath the segment centre (Fig. 2): the first geometry (geometry A) would represent an upwelling more focused under the segment centre, while the other (geometry B) reflects a more sheet-like along-axis upwelling instead. Both geometries are characterized by four parameters: the depth to the top of the hot zone at the segment centre ( $h$ ) and at the segment ends ( $H$ ), the hot zone along-axis length ( $L$ , set to the total length of the segment minus 10 km) and the hot zone across-axis width ( $I$ ) of the cylindrical part of the hot zone. The latter is set equal to 20 km as the geophysical outputs were found to be rather insensitive to this parameter (Gac *et al.* 2003). Thus, for a segment with a given length  $L$ , only the two parameters  $H$  and  $h$  were, in a first stage, allowed to vary for each model and for each geometry (A or B).

The comparison between modelled geophysical outputs and observations is summarized (Fig. 3) in the two-parameter space ( $H$ ,  $h$ ), for three segment lengths (30, 50 and 90 km) and for the two

## GEOMETRY A



## GEOMETRY B

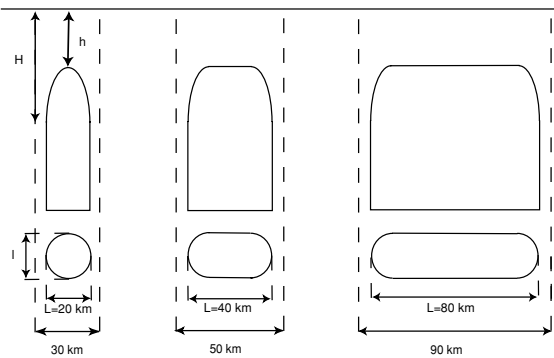


**Figure 2.** Different shapes (geometry and dimensions) of the hot zone considered for 30-, 50- and 90-km-long segments (for each geometry. Top: along-axis vertical section; bottom: view from above). The length  $L$  of the hot zones is 20, 40 and 80 km, respectively, that is 10 km shorter than the segment length. The across-axis width  $l$  of the hot zone is fixed to 20 km at the segment centre.  $H$  is the depth to the top of the cylindrical part of the hot zone,  $h$  the depth to the top of the hot zone. Geometry A simulates a focused upwelling at the segment centre. The width of the hot zone decreases and the depth to the top of the hot zone increases regularly away from the segment centre. Geometry B simulates a sheet-like upwelling of hot material, more evenly distributed along the whole segment. The width of the hot zone and the depth to the top of the hot zone are uniform along most of the segment length and vary rapidly within the outermost 10 km towards segment ends.

geometries A and B. Fig. 3 reveals that, if geometry A is assumed, no ( $H$ ,  $h$ ) parameter couple accounts simultaneously for the three geophysical observables, for the two longer segments (50 and 90 km). Conversely, geometry B succeeds in adjusting simultaneously the three geophysical observables for the three segment lengths, which were tested (30, 50 and 90 km). Moreover the ( $H$ ,  $h$ ) ‘best-fitting domain’ does not significantly vary when any of these segment lengths is considered. Geometry B and ‘best-fit’ values of  $15 \pm 2$  km for  $H$  and  $10 \pm 2$  km for  $h$  will, therefore, be retained for the rest of this study. It is important to note that a simple change in the hot zone along-axis length, with no other dimension and geometry change, succeeds in accounting for the geophysical observations over segments which total length ranges from 30 to 90 km.

The main observation constraining this result is the maximum depths of earthquakes observed at segment centres and segment ends. Microseismicity surveys conducted along several segments of the MAR (Toomey *et al.* 1985, 1988; Kong *et al.* 1992; Wolfe *et al.* 1995; Barclay *et al.* 1993) indeed suggest that earthquakes occur at maximum depths, which are shallowing from  $9 \pm 1$  km beneath segment ends to 2–5 km beneath segment centres, whatever the

segment length. The maximum depth of earthquakes represents the depth of the brittle/ductile transition, and thus corresponds to the depth of the  $500^\circ\text{C}$  isotherm at segment centres (where the oceanic crust is thicker) and to the depth of the  $750^\circ\text{C}$  isotherm at segment ends (where peridotites are frequently outcropping). These isotherm depths are controlled by the depth to the top of the hot zone at the segment centre ( $h$ ) and segment ends ( $H$ ), respectively. As the observed maximum depths of earthquakes do not significantly vary with the segment length, it is therefore, not surprising that the ‘best-fit’ depth to the top of the hot zone was found to be similar for the three different segment lengths. The length of the segment (which equals  $L + 10$  km) is, therefore, the only critical parameter left in our model to influence the segment’s thermal structure.

A longer segment (and consequently a longer hot zone) implies a longer melting zone, and therefore results in a thicker crust beneath segment centres, from 5 km for the shorter segments to 6.2 km for the longer. This is in agreement with observations from seismic refraction experiments conducted on the MAR at  $35^\circ\text{N}$  (Canales *et al.* 2000; Hooft *et al.* 2000), which suggest a slightly thicker crust at the centre of longer segments. A longer hot zone also results in stronger amplitude of the modelled  $\Delta\text{MBA}$  from 10 MGal for the 30-km-long segment to 35 MGal for the 90-km-long segment. Indeed the amplitude of  $\Delta\text{MBA}$  depends on the distance between the segment centre and ends, as the influence of higher densities of the thinner crust at segment ends on the gravity anomaly at the segment centre fades away with increasing segment length. Again this agrees well with gravity observations over MAR segments (Detrick *et al.* 1995; Thibaud *et al.* 1998).

### A consistent thermal structure for the different sample segments: towards a single model of evolution?

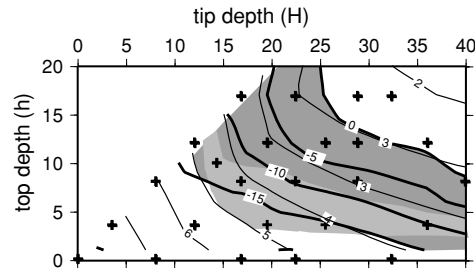
Fig. 4 displays the modelled thermal structure for 30-, 50- and 90-km-long sample segments as resulting from their ‘best-fitting’ hot zone (geometry B, along-axis hot zone 20, 40 and 80 km long, respectively). In each case, three vertical thermal sections are presented:

- (1) across-axis at segment end,
- (2) along-axis and

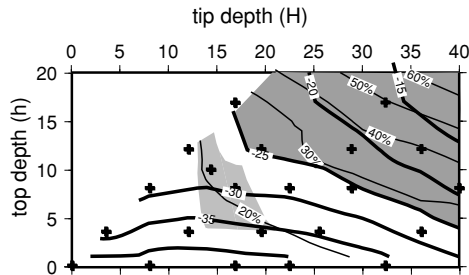
(3) across-axis at segment centre. The thermal structure, resulting from the same simple conceptual model, based on the presence of a permanent hot zone with geometry B under the segment centre, accounts for the geophysical observations over these sample segments of different lengths. This thermal structure is characterized by two different patterns of temperature versus depth, the first of which being valid along most of the segment length (i.e. over a ‘long centre’, corresponding to the cylindrical part of geometry B), the other along the outermost 10 km near the segment ends.

In short, the following picture stands out from our thermal simulation of the ridge segments as described above. The best-fit depth to the top of the hot zone remains almost unchanged when the sample segment length is taken to be between 30 km (short segment) and 90 km (long segment). As a consequence, the across-axis thermal section at the segment centres remains quite the same whatever the segment length. There is no need for higher temperatures or shallower top of the hot zone at the centre of the longer segments to account for the observations. In this respect, the classification between ‘hotter’ and ‘colder’ segments may be misleading and would only reflect the fact that longer segments, associated to a longer—and therefore, more voluminous—hot zone, produce a larger heat output than the short segments.

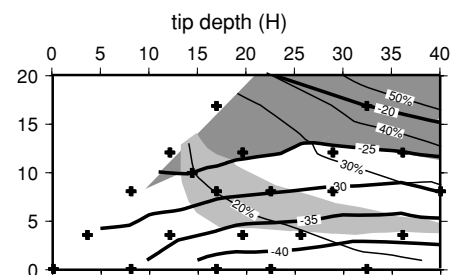
## 30 km-long segment: Geometry A and B



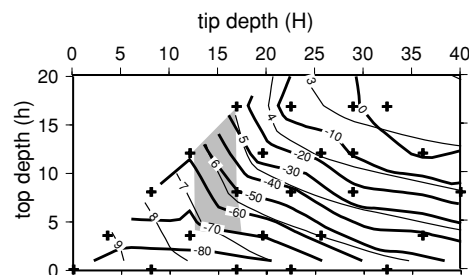
## 50 km-long segment: Geometry A



## 50 km-long segment: Geometry B



## 90 km-long segment: Geometry A



## 90 km-long segment: Geometry B

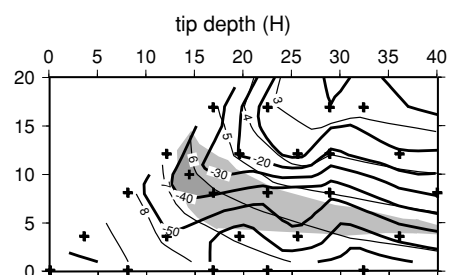


**Figure 3.** Determination of the best geometry and dimensions of the hot zone for three segment lengths (from top to bottom, 30, 50 and 90-km-long segments). Two end-member geometries are considered: geometry A (left) and geometry B (right; see Fig. 2). For each segment length, dimensions  $L$  and  $l$  are fixed and dimensions  $H$  and  $h$  vary (see caption of Fig. 2 for a definition of these parameters). The thermal structure and three related geophysical outputs are simulated for many different values of  $H$  and  $h$  (crosses). As a result, acceptable  $(H, h)$  domains are defined with respect to different criteria. Thick lines show interpolated  $\Delta$ MBA contours and the dark grey area correspond to  $(H, h)$  values, which account for the observed range of  $\Delta$ MBA for each of the three given segment lengths. The light grey area corresponds to  $(H, h)$  values, which account for the maximum depth of earthquakes (i.e. to depths of the  $750^\circ\text{C}$  isotherm, which equal  $9 \pm 1$  km at segment ends and of the  $500^\circ\text{C}$  isotherm, which range between 2 and 5 km beneath segment centres). The two grey areas present no overlap for 50- and 90-km-long segments with geometry A (middle and bottom left), demonstrating that such a hot zone shape cannot account for observations on the earthquake depths and gravity anomalies. Conversely, adequate  $(H, h)$  couples can be found if geometry B is adopted (right). On the plots corresponding to 50-km-long segments (middle), thin lines show interpolated contours for the fraction of extracted liquid reaching the surface, which is required to produce a 6-km-thick crust at the segment centre. The overlap of the two grey areas for the 50-km-long segment with geometry B (middle right) corresponds to a 20 per cent fraction of extracted liquid, a value then used to compute crustal thickness for 30- and 90-km-long segments (which value at segment centre is shown as thin lines on top and bottom plots). The simulated crustal thickness is 4.5 and 6.5 km at the centre of 30- and 90-km-long segments, respectively.

On the basis of off-axis observations, it has been proposed that the length of the segments may systematically vary through time (e.g. Gente *et al.* 1994, 1995). The simple and consistent model obtained with only varying the length of the hot zone strongly suggests that segments of different lengths constitute in fact the different steps of a single evolution process: the axial geophysical characteristics of the segment would progressively evolve from those of shorter segments to those of longer ones, together with the along-axis lengthening of the hot zone. A subsequent shortening of the segment would result from a simultaneous shortening of the hot zone, segment characteristics reversing back from those of longer segments to those of

shorter ones. The three ‘best-fit’ hot zone shapes previously considered in our models for the three sample segments would, therefore, constitute particular stages of a cycle of waxing and waning of the hot zone beneath a slow-spreading ridge segment.

### 3 THERMAL EVOLUTION MODEL

In the previous section, modelling steady-state short, medium and long segments has shown that a simple and single thermal model accounts for the observations over these three segment configurations. We shall now consider a segment which length varies as time goes

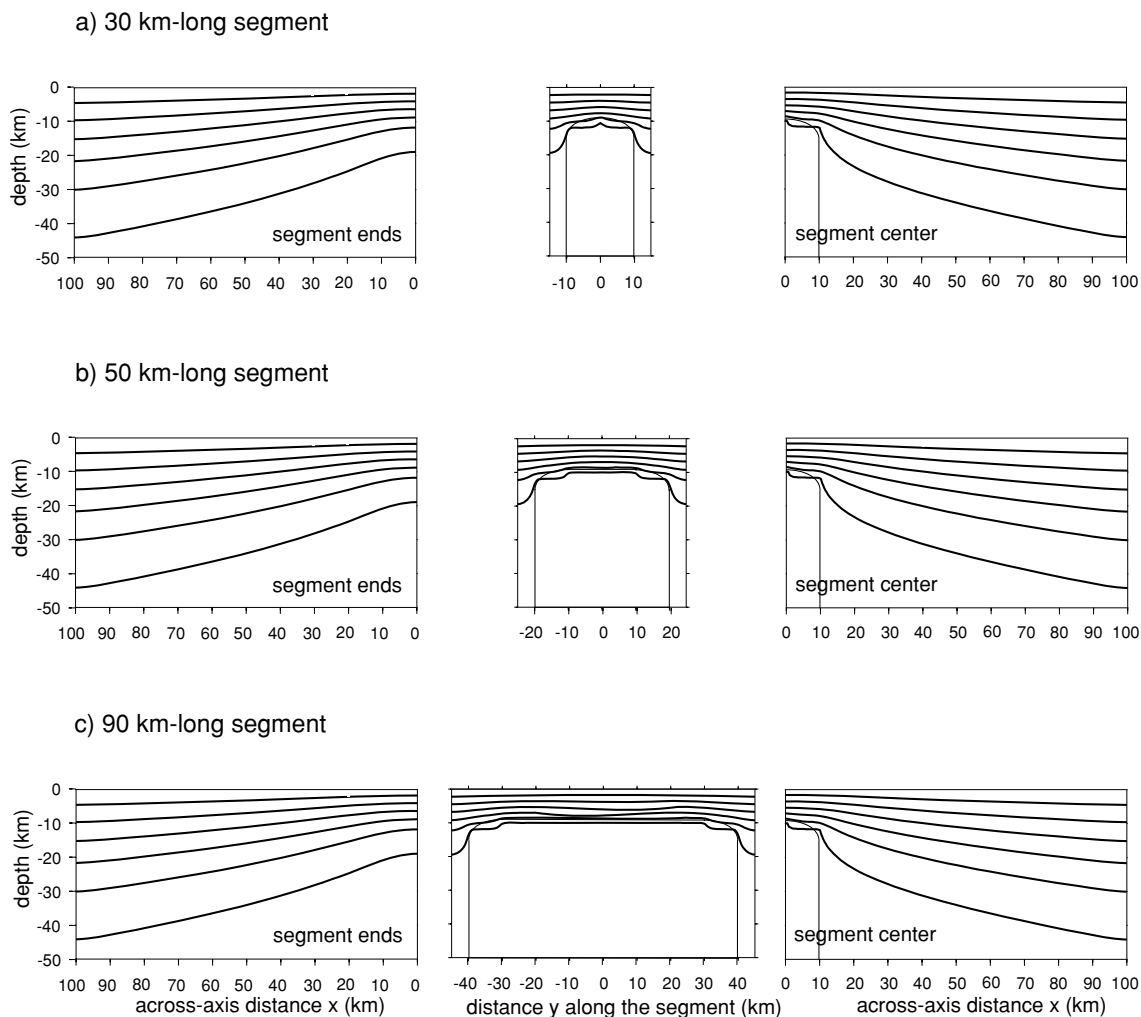


**Figure 4.** Modelled thermal structures for (top to bottom) 30-, 50- and 90-km-long segments, with (left to right) across-axis temperature section at segment ends, along-axis temperature section and across-axis temperature section at the segment centre. Isotherms are contoured at 200°C intervals on all diagrams.

on: the hot zone geometry changes through time and the resulting thermal structure is modelled. At a given stage of this evolution (i.e. for a given segment and hot zone length), the thermal structure is different from the previous steady-state structure, which was computed (in Section 2) from a hot zone with same but time-invariant geometry. The modelled geophysical outputs are, therefore, different from those which were computed in Section 2 for a time-invariant segment. Such differences are expected as it was shown in the previous section that the main parameter, which influences the thermal structure and geophysical parameters of a segment is the time-integrated amount of heat brought to the segment: this amount of heat is obviously different if the length of the hot zone remained constant or has varied through time. The purpose of this section is to determine the optimal evolution, which reproduces the successive geophysical signatures of a segment through time.

### Modelling the hot zone evolution

Let us suppose that the hot zone evolves regularly and passes through the three intermediate stages modelled in Section 2. At first, the hot zone progressively lengthens along the ridge axis from 20 to 80 km, corresponding to 30- and 90-km-long segments, respectively. The lengthening rate is assumed to be constant through time. Then, the

hot zone shortens along the axis till it recedes to its initial length. This successive lengthening and shortening will constitute one ‘cycle’. The thermal evolution will be considered after five full cycles to obtain a meaningful evolution from one cycle to the next, independently of the chosen initial state.

As suggested by the rhomb-shaped areas observed in the bathymetry, the lengthening of a segment is accompanied by the shortening of its neighbours. In this study we consider the simple case of a synchronized phase-opposition evolution: during the time when the hot zone of a segment lengthens along the axis, the hot zones of the adjacent segments simultaneously shorten, and conversely. In fact one segment lengthens and shortens at segment ends symmetrically with its centre kept at a fixed location. Two half hot zones of adjacent segments are considered in the modelling process as the null lateral heat flux boundary condition on across-axis vertical plans passing through both segment centres is expected for a symmetrical geometry and thermal structure with respect to the boundary plan. First the modelled segment axes are supposed aligned, second they are offset. Details about the computational box and boundary conditions can be found in Gac *et al.* (2003).

In these simulations, the evolution is controlled by the durations of lengthening and shortening of the hot zone. As constant-rate lengthening and shortening are considered, these durations can be

expressed in terms of along-axis propagation and recession rates. We shall now try and constrain both parameters for an individual segment surrounded by two adjacent ones, in order to determine the optimal evolution scheme, which better reproduces the geophysical parameters through time.

### The optimal evolution as constrained by the geophysical observables

As shown above, the maximum depth of microearthquake foci and the crustal thickness vary relatively little with the segment length. Moreover, these have only been observed over a few segments along the MAR. On the other hand, the  $\Delta$ MBA amplitude has been measured on about 50 segments. These observed  $\Delta$ MBA values are representative of the different stages of the segments evolution. They will, therefore, be used below as the main constraint on the parameters governing the hot zone evolution. So, only the modelled  $\Delta$ MBA will be presented in detail below.

The presence of an axis offset between adjacent segments results in a much more efficient cooling near their ends, compared to the case of aligned segments. This cooling changes the thermal structure of the segment ends and their geophysical signature. To test the influence of an axis offset, five offset lengths (0, 10, 20, 30 and 40 km), representative of the whole range of offsets observed along the MAR, were considered in the simulations.

#### Influence of the propagation rate

In the 20–24°N zone of the MAR (cruise SEADMA), the relative orientation of oblique discontinuities and ridge axis observed on seafloor topography is less or very close to 45° (Gente *et al.* 1995) and suggests that the along-axis propagation rate and across-axis half-spreading rate are of the same order, that is, 1 cm yr<sup>-1</sup>.

We have tested values between 0.5 and 1 cm yr<sup>-1</sup>. For small rates (less than 1 cm yr<sup>-1</sup>), the hot zone lengthens and shortens for longer periods, nevertheless the additional heat supply from the hot zone does not have enough time to diffuse efficiently. The thermal evolution remains similar whatever the along-axis propagation rate within the adopted range. In the simulations reported below we have, therefore, adopted the same value for both along-axis propagation and half-spreading rates. The duration of lengthening is then 3 Myr for a half-segment, which length passes from 15 to 45 km.

#### Influence of the hot zone shortening duration

For the shortening of the hot zone, two ways may be considered

- (1) nothing is imposed about the hot zone except its final length, so it progressively cools by heat conduction (called ‘instantaneous shortening’ in the following)
- (2) the rate of shortening is imposed and the hot zone passes through imposed intermediate stages.

The  $\Delta$ MBA versus segment length is plotted on Fig. 5, for two extreme values of the duration of the shortening period: 0 Myr (instantaneous shortening) and 3 Myr (the shortening lasts as long as does the lengthening), in three cases:

- (a) aligned segments,
- (b) small axis offset (10 km offset) and
- (c) large axis offset (40 km offset). The observed  $\Delta$ MBA (thin open circles) and the corresponding linear trend (dotted line) are also

shown. The modelled  $\Delta$ MBA (symbols connected by a line) have been computed at six intermediate stages (i.e. every Myr) through one cycle of evolution (i.e. a lengthening episode followed by shortening).

### Aligned segments

We shall first discuss the results obtained for aligned segments, and then extend these results to offset segments. It is worth noting that the extra heat brought to the system by the hot zone lengthening will propagate along-axis slower than the hot zone itself. The resulting temperature increase is more restricted to the vicinity of the hot zone than in the steady-state segment model (Section 2), because heat has no time to diffuse away from the hot zone.

Because the crustal thickness varies little at the segment centre (as seen in Section 2), the  $\Delta$ MBA depends mainly on the crustal thickness at segment ends, hence on the thermal structure and crustal production at segment ends. Indeed, the thinner the crust is at the segment ends, the higher is the density contrast between the segment ends and the centre and consequently stronger is the modelled  $\Delta$ MBA. The thermal structure of the segment ends results from:

- (1) the distance from both adjacent hot zones: the shorter it is, the warmer is the segment end and greater is the crustal production and
- (2) the location of both hot zones in the past as this has consequences on conductive heat diffusion.

A fast lengthening of the segment allows little for heat diffusion outside the imposed hot zone, and at the segment ends the heat supply from the central part of the hot zone decreases through time. On the other hand, the segment ends propagate into areas previously occupied by the hot zones of the adjacent segments, which increasingly supply the first segment with heat as time goes. Therefore, the thermal regime at segment ends results from both heat supplies, the variations of which are more or less balanced within a cycle.

For a rapid shortening, this regime is colder than for longer-lasting shortening. As the duration of shortening increases from 0 to 3 Myr, the crustal thickness at segment ends increases from 1.5 to 3 km. The  $\Delta$ MBA consequently decreases and becomes comparable to the observed mean trend (Fig. 5a). The ‘best-fit’ shortening duration is found to be 3 Myr. Each cycle thus includes a lengthening phase and a shortening phase of same duration.

### Offset segments

Similar results are obtained in the case of offset segments. For small values of the offset (10 or 20 km), there is little difference from the case of aligned segments (Fig. 5b): both neighbouring hot zones are close to each other and the variations of heat supplies from adjacent segments still compensate near segment ends.

This is no longer the case for larger offset values (30 or 40 km). The two hot zones are far enough from each other, so that the thermal regime of the segment ends almost entirely depends on the heat supply from the hot zone located beneath the centre of the corresponding segment. The heat supply and crustal production at segment ends are low during the segment lengthening and becomes higher when the segment shortens, in relation to the time-shift between the fast propagation of the hot zone and the comparatively slower heat diffusion. During a cycle, the crust at segment ends is 3 km thick when the segment is short (resulting in a small  $\Delta$ MBA,

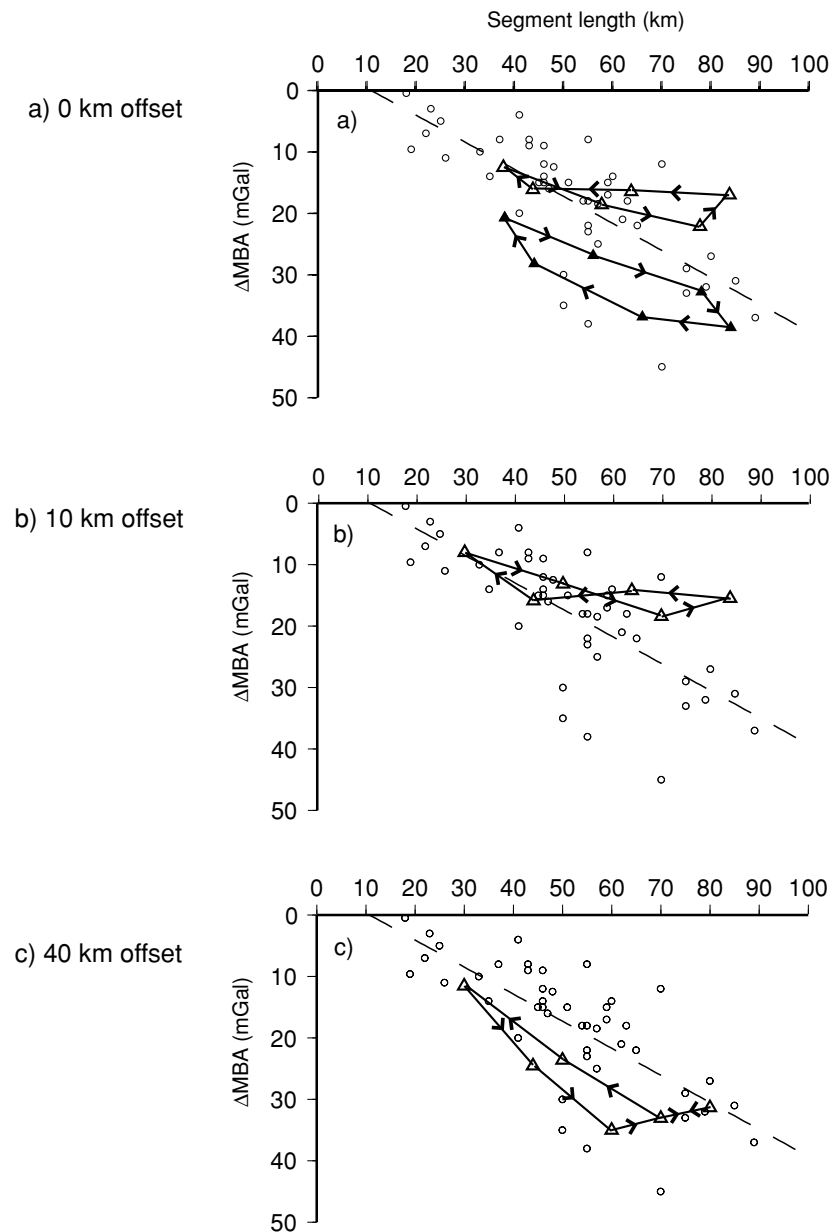


**Figure 5.** Modelled  $\Delta\text{MBA}$  versus segment length during a cycle of evolution, for various segment offsets (top to bottom: aligned segments, 10 and 40 km offsets). Connected symbols show the modelled  $\Delta\text{MBA}$  at each 1 Myr time step of the segment evolution. Open triangles correspond to equal, 3-Myr-long lengthening and shortening of the hot zone. For aligned segments, filled triangles correspond to a 3-Myr-long lengthening and an instantaneous shortening of the hot zone. For comparison, open circles show the observed  $\Delta\text{MBA}$  between  $15^\circ$  and  $40^\circ\text{N}$  along the MAR (Thibaud *et al.* 1998) and the dotted line shows the linear regression trend.

Fig. 5c). It becomes thinner,  $\sim 1$  km, when the segment lengthens and thickens again to 3 km when the segment shortens back.

#### The optimal evolution

Whatever the offset value, the best fit between modelled and observed  $\Delta\text{MBA}$  is obtained for equal durations of the hot zone shortening and lengthening periods (i.e. close to 3 Myr). Besides the  $\Delta\text{MBA}$ , other geophysical outputs are also computed for the five values of the axis offset (0, 10, 20, 30 and 40 km). The thermal structure of the segment centre varies very little through a cycle of evolution, whatever the axis offset. The same holds for the temperature-dependent processes at the segment centres: the  $500^\circ\text{C}$  isotherm

remains at a depth close to 4 km (within the observed range of 2–5 km for the maximum depth of microearthquake foci) and the crustal thickness remains close to 6 km. At segment ends, because the cooling is a little more efficient, the  $750^\circ\text{C}$  isotherm slightly deepens during the hot zone lengthening, especially for greater values of the offset, but its depth remains in the range of  $9 \pm 1$  km, as observed for the depth of microearthquake foci. The crustal thickness varies between 1 and 3 km as stated above.

In short, our model of thermal evolution succeeds in explaining the axial characteristics ( $\Delta\text{MBA}$ , crustal structure and maximum depths of earthquakes) of the various MAR segments, the entire range of observed axis offsets between adjacent segments being considered.

#### 4 OFF-AXIS GEOPHYSICAL SIGNATURE OF THE THERMAL EVOLUTION

Fig. 6 shows the geophysical fields observed over the off-axis region of the MAR between 21°30'N and 22°30'N, to be used for comparison with the model outputs. Rhomb-shaped patterns stand out in these observations and depict the segment evolution. These patterns suggest that the MAR 21°40'N segment (TAMMAR) has lengthened both northwards, in line with its northern neighbour, and southwards at the expense of its southern neighbour, which is offset by 40 km westwards.

In order to try and model the observed rhomb-shaped patterns, we have computed the off-axis topography, gravity (MBA) and magnetic anomalies, which result from the thermal evolution model after offsets of various lengths (0, 10, 20, 30 and 40 km) were introduced between adjacent segments. The simpler case of aligned segments was first considered, then the more complex case of offset segments.

##### Aligned segments

###### *Off-axis crustal thickness*

Off-axis topography, gravity and magnetic anomalies are mainly controlled by the off-axis crustal structure, especially by the crustal thickness variations. Fig. 7(a) represents the crustal thickness pattern resulting from the evolution of two aligned adjacent segments. On Fig. 7(a) and on the subsequent figures, the segment termed 'segment #1' is located in the upper part of the figure and the adjacent 'segment #2' is in the lower part. As spreading goes on, the off-axis region (which extends between distances  $x = \pm 60$  km to  $x = 0$ ) reflects the evolution of both segments through a complete cycle from time  $t_0$  to time  $t_0 + 6$  Myr. At the beginning of the cycle  $t_0$  ( $x = \pm 60$  km) segment #1 is short, then it progressively lengthens till  $t_0 + 3$  Myr ( $x = \pm 30$  km) and returns to its initial length at the end of the cycle ( $t_0 + 6$  Myr,  $x = 0$ ). Such a lengthening and shortening is achieved at the expense and profit (respectively) of the adjacent segment #2. Lengthening and shortening of the hot zones generate an along-axis motion of the segment ends, which correspond to an area of thinner crust. The off-axis traces of the past positions of the segment ends form rhomb-shaped patterns in the crustal structure.

###### *Topography and gravity*

Figs 8(a) and (b) show the isostatic topography and MBA computed for time  $t_0 + 6$  Myr, after the two segments have gone through a complete 6 Myr cycle. Both these fields result from variations in the modelled density structure.

Our model only allows the computing of the isostatic topography, assuming that local compensation is achieved. Isostatic topography is the contribution to topography of density variations from several origins: thermal expansion, presence of liquid in the melting zone, density contrast between crust and mantle, and serpentinization of peridotites. It should be noted that other important contributions to the topography have not been taken into account, such as the tectonics due to the brittle rheology of the upper lithosphere. Indeed, tectonic processes essentially produce topography (such as the axial valley and abyssal hills) at a smaller scale than those resulting from the segment's thermal evolution and, therefore, probably only bring little useful constraints at the scale of our model results. Past segment ends may probably have peculiar rheologies, because of their colder thermal structure, thinner crust and the occurrence of serpentinized peridotites. Taking these peculiar rheologies into account would

require mechanical modelling, which is beyond the scope of the present study. Keeping these limitations in mind, the contribution of density variations to the topography is considered as a good approximation to the off-axis medium-wavelength bathymetry pattern, as it results from our thermal evolution model.

Off-axis, the density variations are mainly due to the variations in the crustal thickness and, to a lesser extent, due to the serpentinization of peridotites, to temperature changes and to the presence of liquid in the melting zone. Densities increase away from the axis with lithosphere cooling, causing a deepening of the ocean floor and a progressive increase in the MBA. Consequences of crustal density variations are clear along the past traces of segment ends, which limit rhomb-shaped areas in off-axis regions. In these areas, the simulation predicts a thin crust underlain by serpentinized peridotites. Our model successfully accounts for the rhomb-shaped pattern observed off-axis along the MAR in the topography and in the MBA (Figs 6a and b). From the centre of the rhomb-shaped areas to their boundaries, the modelled topography deepens by 1000 m and the modelled MBA increases by 10 mGal, values that are comparable to the observed ones (Fig. 6).

###### *Magnetic anomalies*

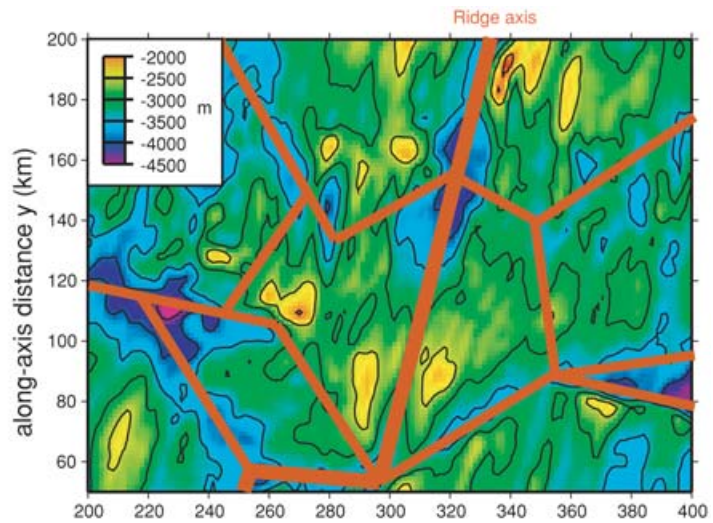
Fig. 8(c) represents the computed magnetic anomaly pattern at the end of one complete cycle of evolution of the two segments (at time  $t_0 + 6$  Myr). These anomalies are easily deduced from the distribution of magnetization in the crust and uppermost mantle, the acquisition of which through time is simulated from the thermal evolution model, the resulting crustal structure and petrological distribution, and the magnetic properties of rocks (following the method detailed in: Arkani-Hamed 1989; Dymant & Arkani-Hamed 1995; Dymant *et al.* 1997; Gac *et al.* 2003).

Four kinds of rocks which bear magnetic minerals and, therefore, carry a magnetization are considered:

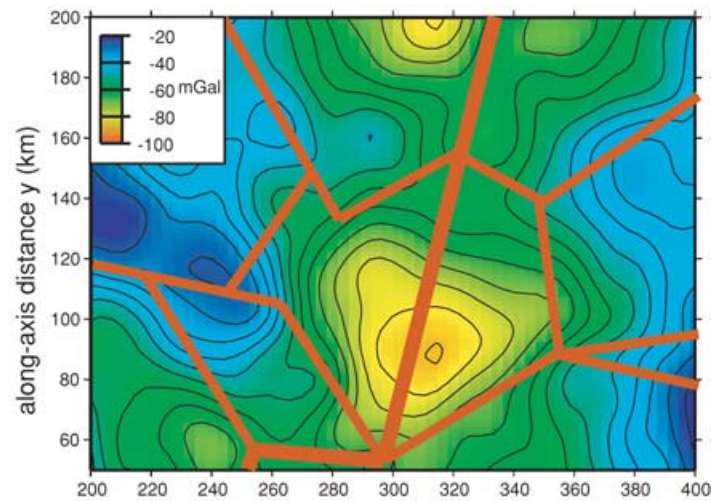
- (1) extrusive,
- (2) intrusive basalts,
- (3) olivine gabbros and
- (4) serpentinized peridotites.

The first three layers have thicknesses proportional to the total crustal thickness (0.5, 1.5 and 4 km, respectively, for a reference 6-km-thick crust). The presence of serpentinized peridotites is controlled by temperature and by the presence of water. The magnetization is the sum of two components: an induced magnetization parallel to the present magnetic field and depending on the present thermal structure, and a thermoremanent magnetization acquired by the rocks when they cooled through their Curie temperature during the thermal evolution. The induced magnetization is weak and is considered negligible for basalts and gabbros. It is comparable to the remanent magnetization and was taken into account for serpentinized peridotites. Maximum thermoremanent magnetization intensities of 10, 0.5, 1 and 5 A m<sup>-1</sup> have been adopted for extrusive and intrusive basalts, olivine gabbros and fully serpentinized peridotites, respectively (Bleil & Petersen 1983; Kent *et al.* 1978; Pariso & Johnson 1993; Bina & Henry 1990). The thermoremanent magnetization depends on the thermal history of the rock and the sequence of geomagnetic reversals during this history. The Fe–Ti enrichment of basalt, a consequence of a higher fractionation degree, results in a 2.5-fold increase of the basalt magnetization at segment ends with respect to segment centres (Weiland *et al.* 1996). In addition, the magnetization of extrusive basalt decreases exponentially with age as a result of the progressive alteration of

a) observed bathymetry



b) observed MBA



c) observed magnetic anomalies

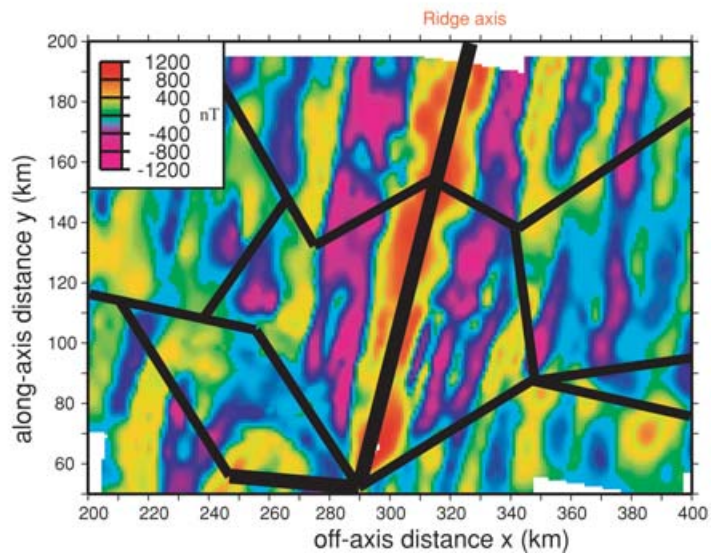


**Figure 6.** Off-axis observations along segment TAMMAR, on the MAR at  $21^{\circ}40'N$ . This segment exemplifies the differences between aligned segments to the North, and segments offset by 40 km to the South, for (a) bathymetry (after Gente *et al.* 1995), (b) MBAs (after Maia & Gente 1998) and (c) magnetic anomalies (after Ravilly 1999). The present ridge axis and offsets are shown as thick lines. The traces of past segment ends and the limits of transferred crust areas appear as thinner lines.

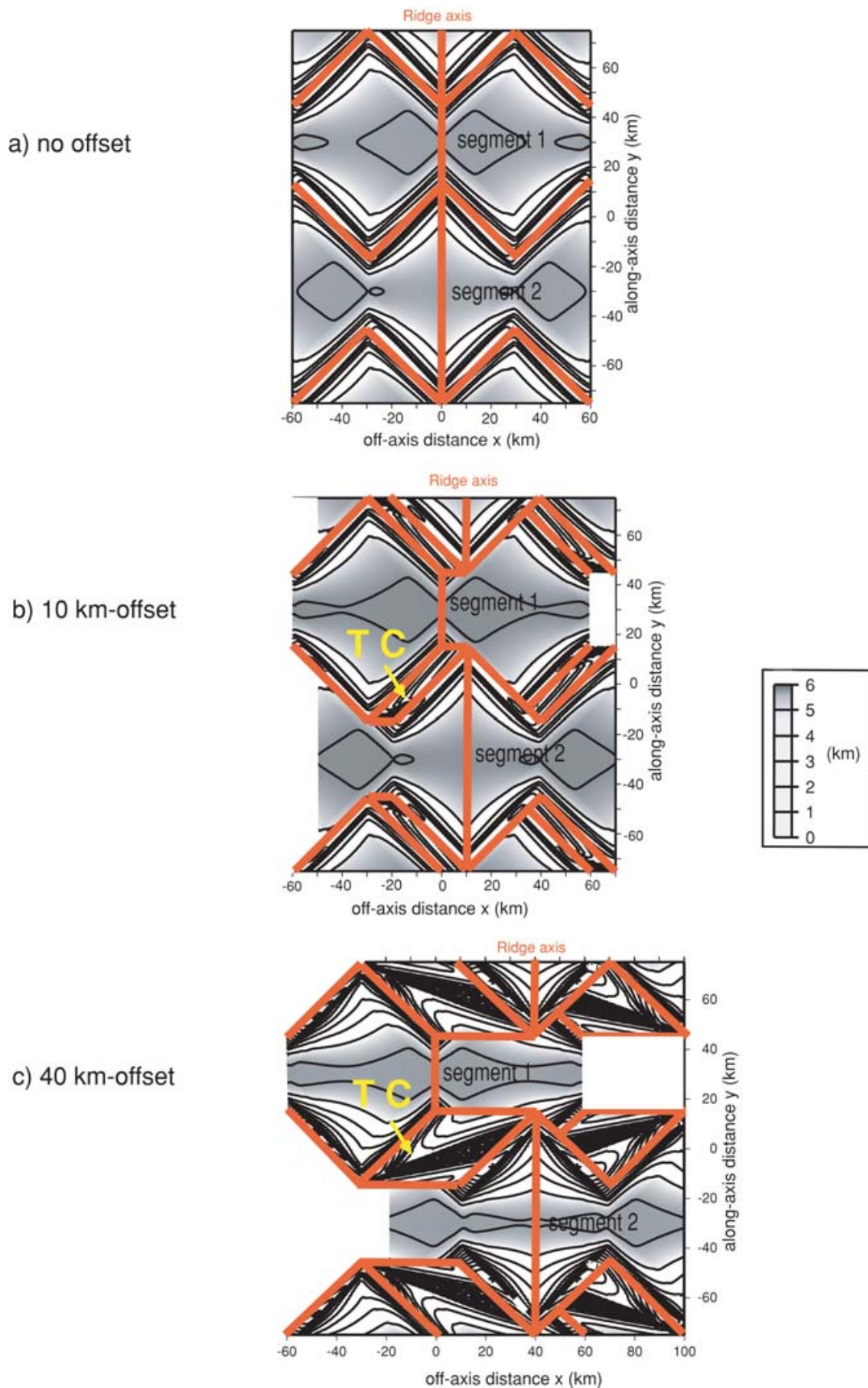


**Figure 7.** Modelled crustal thickness variations for three offset lengths, as they result from the evolution of two adjacent segments through a complete cycle. The present ridge axis and offsets are shown as thick lines. The traces of past segment ends and the limits of transferred crust (TC) areas also appear as thick lines.

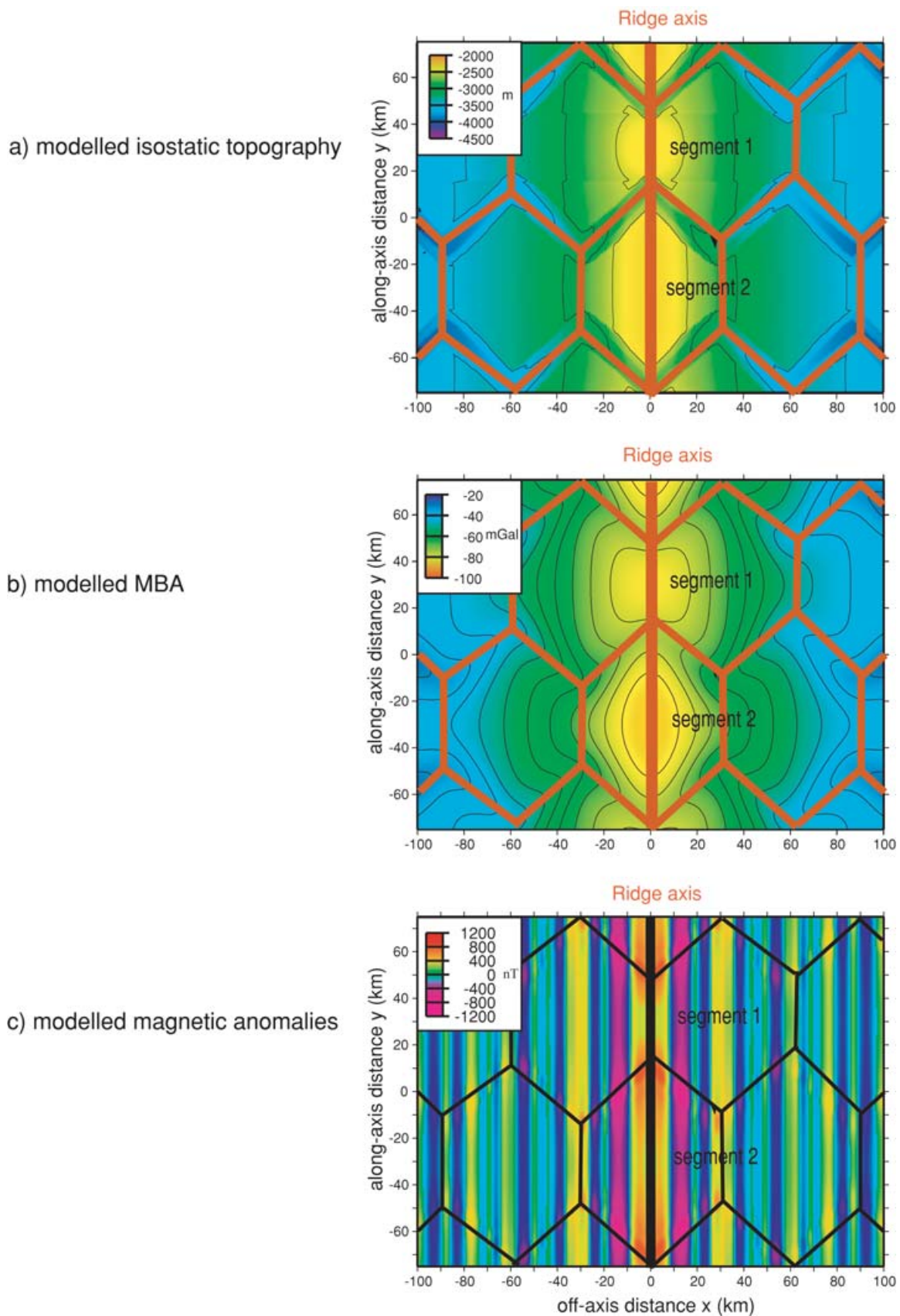


**Figure 8.** Modelled isostatic topography, MBAs and magnetic anomalies for aligned segments, after a complete cycle of evolution. For instance, the segment at the top of the modelled box, initially at a minimum length, has lengthened during 3 Myr, then shortened to its initial length during the next 3 Myr. The present ridge axis is shown as thick lines. The traces of past segment ends appear as thinner lines.

titanomagnetite, the main magnetic mineral of extrusive basalts. This decrease causes the anomaly amplitude to decay for the last 10 Myr (Irving 1970; Marshall & Cox 1972). The magnetization of serpentinized peridotites varies with the degree of serpentinization, a function of temperature and water content (hence depth). A more complete description of the magnetization modelling is given in Gac *et al.* (2003).

The simulated distribution of the magnetization, therefore, takes two along-axis variations into account, the Fe–Ti enrichment of basalts towards segment ends and the presence of serpentinized peridotites beneath the thinner crust at segment ends. Both effects increase the remanent magnetization and the latter also increases the induced magnetization at segment ends, resulting in amplitudes of the axial anomaly twice higher at segment ends than at segment centre (Ravilly *et al.* 1998; Gac *et al.* 2003). Seafloor spreading subsequently displaces off-axis the magnetization patterns acquired at the axis and traces of the past segment ends are clearly marked in the magnetic anomalies.

In the case of aligned segments, the crust is 3 km thick along segment ends and their off-axis traces (Fig. 7a). Below this depth, the peridotite is weakly serpentinized and its magnetization is low, so basalt and olivine gabbro are the main contributors to the magnetic signal. As noted above, the remanent magnetization of basalt is 2.5 times higher at segment ends than at segment centres. If this basalt has been emplaced during a period of reversed geomagnetic field, its magnetization is negative and lower at past segment ends than at past segment centres. Conversely, if the basalt has been emplaced during a normal geomagnetic period, its magnetization is positive and higher at past segment ends than at past segment centres. The past segment ends are thus characterized by stronger magnetization contrasts and, therefore, by stronger, either more negative or more positive, magnetic anomalies. So strong magnetic anomaly amplitudes underline the off-axis past segment geometry of aligned segments, both on simulated (Fig. 8c) and on observed magnetic anomalies patterns (see Fig. 6c, southern boundary of the northernmost segment).

## Offset segments

### *Transferred crust and off-axis crustal thickness*

With respect to the previously considered case of aligned segments, the presence of an offset and its along-axis motion through time, modify the modelled off-axis crustal structure and associated geophysical fields. Indeed the geometry of our simulation is that of a ‘propagating rift’ as was first observed on the Coco-Nazca spreading centre (Hey 1977; Hey *et al.* 1980) and, later, on other mid-ocean ridges (e.g. Wilson *et al.* 1984; Dyment 1993, 1998; Lonsdale 1994; Phipps Morgan & Sandwell 1994). Unlike the case of aligned segments, the lengthening segment propagates within aged crust and this propagation results in the transfer, to the other ridge flank, of crust which was initially emplaced on one flank of the shortening segment (area marked TC, for transferred crust, in Figs 7b and c). The transferred crust forms a parallelogram area, the surface of which depends on both the offset length (in the across-axis direction) and the propagation rate (in the along-axis direction). In the example considered in this study (propagation and half-spreading rates of  $1 \text{ cm yr}^{-1}$ ) this surface reaches  $300 \text{ km}^2$  for a 10 km offset (Fig. 7b) and  $1200 \text{ km}^2$  for a 40 km offset (Fig. 7c). Because the ridge segment propagation is progressive, the transferred crust (between the propagating and receding segment ends) is progressively

deformed. Simple geometrical considerations show that a ridge-parallel feature becomes oblique by  $\arctan(2R_s/R_p)$ ,  $R_s$  and  $R_p$  being the half-spreading rate and propagation rate, respectively, or  $63^\circ$  with the chosen parameters (see Figs 9c and 10c).

The cyclic behaviour of our evolution model further complicates crust transfers, as a small part of the transferred crust area is in fact ‘retransferred’ crust, that is, which has already been transferred to the other flank on the previous cycle of evolution. The amount of ‘retransferred’ crust corresponds to the truncated triangle at the end of the transferred crust parallelograms, towards the ridge axis: while it is small indeed in the case of small offsets (Figs 7b and 9), it can become quite large in the case of greater axis offsets (Figs 7c and 10). Such a case of retransferred crust, predicted by our model, has still to be reported, probably because our ‘perfectly cyclical evolution model’ is an oversimplification of more complex natural configurations.

An episode of propagation creates three oblique structures: the pseudo-faults limit the crust created at the propagating and receding segments, with

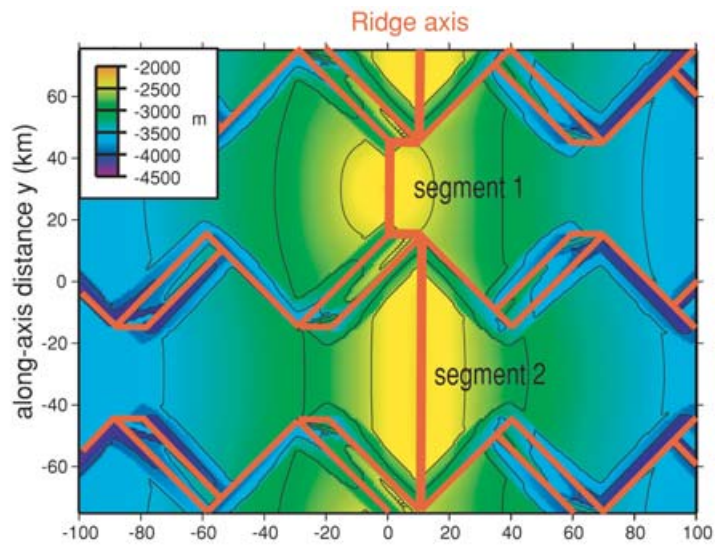
- (1) the inner pseudo-fault on the side of the transferred crust area
- (2) the outer pseudo-fault on the other side and
- (3) the failed rift separates the transferred crust from normal crust created at the receding segment. Past segment ends of the propagating segments align along the inner and outer pseudo-faults, and those of the receding segment along the failed rift.

Fig. 7 shows the crustal thickness resulting from the evolution of two adjacent segments which axes are offset by 10 km (Fig. 7b) and 40 km (Fig. 7c). Both pseudo-faults and the failed rift are underlain by a thin crust, as could be expected for past segment ends. The transferred crust area is comparatively thicker, although our modelling is probably over simplistic as it does not consider any tectonic effect. For the larger offset (Fig. 7c), this area is obliquely cut across by a corridor of thinner crust, also a trace of past segment ends, which separates the genuine transferred crust from retransferred crust. The wakes of thinner crust left by past segment ends present some differences, as the crust is thicker at the past ends of shortening segments than of lengthening segments (see Section 3). The difference is weak for small axis offsets (Fig. 7b) but becomes important, 1.5 km, for a 40 km offset (Fig. 7c).

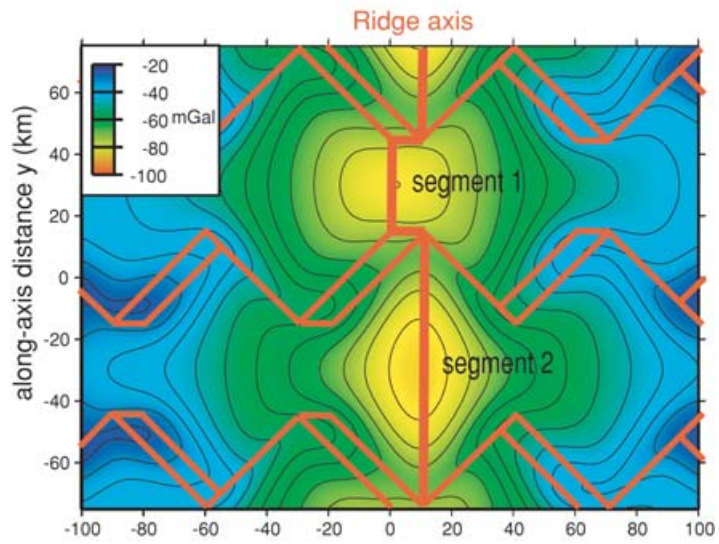
### *Isostatic topography and MBA*

The isostatic topography and MBA are modelled at the end of a complete cycle, assuming 10 and 40 km offsets (Figs 9a and b, 10a and b). As was the case for aligned segments, past segment ends clearly stand out on both modelled topography and MBA. From the centre of rhomb-shaped areas to their boundaries the modelled isostatic topography deepens by 1000 m and the modelled MBA increases by 15 mGal, in good agreement with the observations (Figs 6a and b). This is also the case for the outer pseudo-fault, marked by a narrow depression on the side of the propagating segment and a distorted ‘bull’s eye’ (Figs 9a and b). The transferred areas, with past segment ends and thinner crust on both sides, are similarly bounded by two parallel narrow depressions, with similar depths (i.e. similar crustal thicknesses) for a 10 km offset. For larger offsets, the failed rift, that is, the past ends of the receding segment, has a thicker crust ( $\sim 3\text{--}4 \text{ km}$ ) than the pseudo-faults, that is, the past ends of the propagating segment (0.5–1.5 km), and the narrow depression associated with the pseudo-faults is, therefore, deeper than that of the failed rift. For a 40 km offset (Fig. 10a) an additional depression runs across the

a) modelled isostatic topography



b) modelled MBA



c) modelled magnetic anomalies

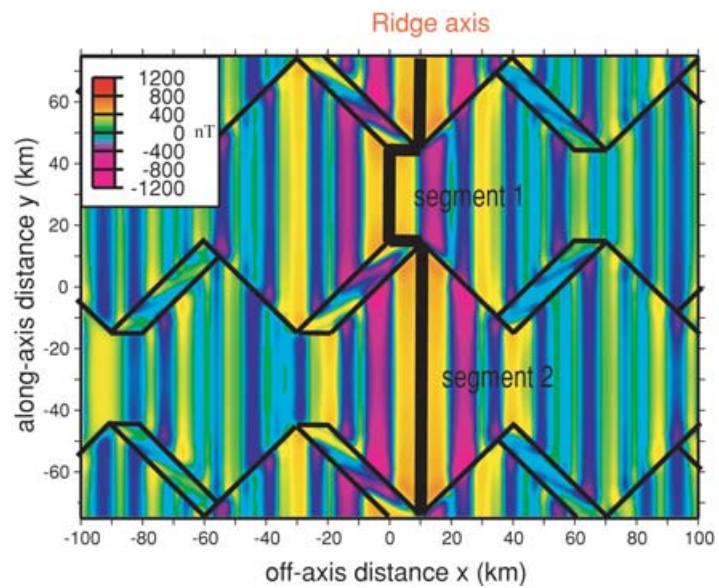


**Figure 9.** Same as Fig. 8, but segments are offset by 10 km. The present ridge axis and offsets are shown as thick lines. The traces of past segment ends and the limits of transferred crust areas appear as thinner lines.

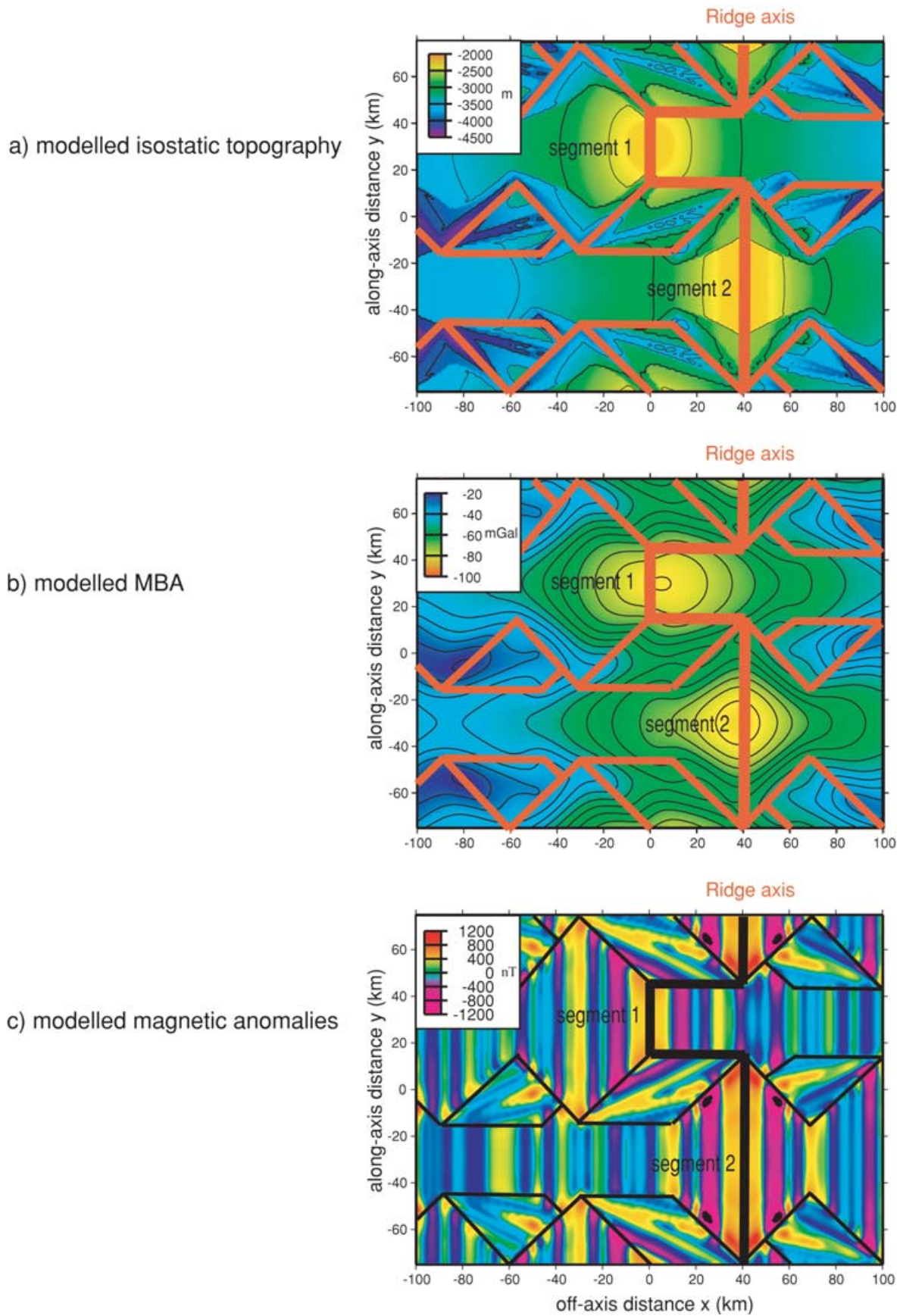


**Figure 10.** Same as Fig. 8, but segments are offset by 40 km. The present ridge axis and offsets are shown as thick lines. The traces of past segment ends and the limits of the transferred crust areas appear as thinner lines.

transferred crust parallelogram and corresponds to an older trace of the segment end, which isolates the retransferred crust. So the transferred crust areas appear particularly complex, displaying one or two topographic highs surrounded by elongated 500–1000-m-deep troughs trending along one or two oblique directions. In the transferred areas, the crust is thinner in average than elsewhere and the associated gravity signal displays a local high, with an amplitude of about 10 mGals for a 10 km offset (Fig. 9b) and more than 20 mGal for a 40 km offset (Fig. 10b). The gravity picture is further complicated by the different ages of the various crustal units, the transferred crust area being younger than the crust located in the symmetrical area with respect to the ridge axis. The asymmetry of crustal thickness and age, hence of the density distribution, results in significant distortion in the contours of the MBA gravity ‘bull’s eye’ centred on the segment. For example, the ‘bull’s eye’ low associated with the shorter segment is laterally displaced by ~5 km towards the transferred crust area (Fig. 10b).

Now, as concerns the observations, a transferred crust parallelogram is observed in the bathymetry southwest of segment TAMMAR (Fig. 6a) as a consequence of the southward propagation of the segment. The observed evolution of the segments in the area and their interrelation are less organized than in our simulation, and no retransferred crust is actually observed. The southward propagation of segment TAMMAR began 4.5 Myr ago, following a period with a stable fracture zone offset (Gente *et al.* 1994, 1995). The failed rift (i.e. the southwestern limit of the transferred crust parallelogram) is marked by a depression that may correspond to the one which our simulation predicts. Similarly, another narrow depression is observed to the southeast on the outer pseudo-fault. However, no depression is observed on the inner pseudo-fault, possibly because the tectonic deformation undergone by the transferred crust is not considered by our model. Isobaths and structures within the transferred area follow an oblique trend, close to the orientation that axis-parallel features—abyssal hills or reactivated faults—should follow after its transfer and deformation. The MBA displays a local high centred on the transferred crust area and the ‘bull’s eye’ associated with the segment centre presents a triangular shape, which emphasizes the southward propagation of the segment (Fig. 10b).

#### Magnetic anomalies

Figs 9(c) and 10(c) represent the modelled magnetic anomalies after a complete cycle of evolution, for 10 and 40 km offsets, respectively. The anomalies show oblique offsets, the pseudo-faults, separating rhomb-shaped areas in which the anomalies are parallel to the ridge axis and the geomagnetic polarity sequence is continuous. The area of transferred crust between the inner pseudo-fault and the failed rift is marked by oblique magnetic anomalies, which follow the orientation of features that were initially ridge parallel and subsequently deformed (Figs 9c and 10c). Similar oblique magnetic anomalies are observed, although subdued, within the deformed area southwest of segment TAMMAR (Fig. 6c).

In terms of along-axis variations, a notable difference with the case of aligned segment is the fact that the crust may be quite thin along segment ends and their off-axis traces (Figs 7b and c), and that the contribution of serpentinized peridotite may be significant. Because it bears comparable induced and remanent magnetizations, it either adds a null contribution if the rocks have been emplaced at segment ends during a period of reversed geomagnetic field, or a positive contribution if they have been formed during a normal period. The only effect of serpentinized peridotite is, therefore, to further increase the high magnetic anomaly amplitudes at segment

ends for crust formed during a normal polarity interval (Figs 9c and 10c).

## 5 CONCLUSION

In a previous study (Gac *et al.* 2003), we have modelled the 3-D thermal structure of a medium-size (50 km), steady-state, slow-spreading ridge segment. This model accounts for the variations along the axis of the MAR, of thermal-related geophysical observables—maximum depth of the earthquakes, crustal structure, gravity and magnetic anomalies. The present paper extends the focus of our previous study by addressing

- (1) the important variability of the segment length, which may reflect either the existence of different types of segment—a typology of ‘hot’ versus ‘cold’ segments was previously proposed—over different steps in the evolution of a single type and
- (2) the off-axis bathymetry and geophysical observations as reported on the MAR flanks.

In a first step, we applied the modelling technique, as was previously developed for a 50-km-long segment to a shorter (30 km) and a longer (90 km) segment. The thermal model is based on the presence, beneath the segment centre, of a permanent hot zone, which shape (geometry and dimensions) is fitted to account for the geophysical observables. We have tested two end-member geometries simulating either a mantle upwelling focused under the segment centre, or a more sheet-like one, distributed along the axis. Only the latter, with a constant section and a flat top ~10 km deep along most of the segment length, succeeds in adjusting simultaneously the three geophysical observables that were considered. The same parameters (except the length of the hot zone) apply for the 30-, 50- and 90-km-long segments, and no variation either in temperature or in the depth to the top of the best-fitting hot zone is required. The modelled thermal structure beneath the segment centre remains identical whatever the segment length and cannot be used to distinguish between ‘hot’ and ‘cold’ segments: there is no ‘cold’ or ‘hot’ segment in terms of temperature. Conversely, the notion of ‘cold or hot’ segment only relates to the total heat supplied by the segment: a longer hot zone simply brings in more heat than a shorter one.

This result strongly suggests that the various ridge segments observed along the MAR only differ by the along-axis length of their hot zone and represent different stages of a single evolution process. Such a hypothesis has already been proposed on the basis of oblique discontinuities and rhomb-shaped areas observed off-axis on the MAR. Following this line, we have developed a quantitative model of evolution based on successive cycles of lengthening and shortening of the hot zone. The modelled geophysical outputs (maximum depth of the earthquakes, crustal thickness, along-axis variations of both gravity and magnetic anomalies) best account for the MAR observations when segment shortening and lengthening periods are of similar duration and when along-axis propagation and recession rates are equal to the half-spreading rate. In off-axis areas, our thermal evolution model simulates isostatic topography and gravity anomaly (MBA) patterns, which are the traces of past segment ends. These patterns delineate rhomb-shaped areas similar to those which have been observed along the MAR. Any significant offset between adjacent segments results in the transfer of crust emplaced on one flank of the receding segment to the other flank by the propagating segment. Although tectonics and deformation (i.e. formation and propagation of cracks in the young lithosphere) are not taken into account by our model, simulated geophysical fields (isostatic topography, gravity and magnetic anomalies) show many similarities with

detailed observations over the 21°40'N (TAMMAR) segment of the MAR.

To summarize, this study has shown quantitatively that simple length variations of the hot zones beneath the segment centres succeed in accounting for the observed thermal evolution and related geophysical characteristics of MAR segments. Our model, based on conductive and advective heat transfer, successfully predicts many geophysical observations, suggesting that the mechanical propagation may only be a consequence of thermal processes—that is, the lengthening of the hot zone. Hot zone length variations would in turn be due to fluctuations in the supply of mantle material. If the mantle supply increases, the emplacement of new oceanic crust would not be efficient enough to absorb the additional material that would, therefore, expand along-axis, in the direction of least mechanical resistance. Conversely, if the mantle supply wanes out, a long hot zone could not be maintained and would then have to shorten.

## ACKNOWLEDGMENTS

This work was partially funded by CNRS-INSU in the Program DORSALES 'Imagerie géophysique de la lithosphère et du manteau'. SG acknowledges support for his PhD work through a research fellowship from the French Ministry of Education and Research. We also thank Dr K. Wang and an anonymous reviewer for helpful suggestions, which resulted in improving the paper's organization. This is IUEM contribution n° 976 and IPGP contribution n° 2096.

## REFERENCES

- Arkani-Hamed, J., 1989. Thermoviscous remanent magnetization of oceanic lithosphere inferred from its thermal evolution, *J. geophys. Res.*, **94**, 17 421–17 436.
- Barclay, A.H., Toomey, D.R., Purdy, G.M. & Solomon, S.C., 1993. FARA microearthquakes experiments III: results from the Mid-Atlantic Ridge at 35°N, *AGU Fall meeting*, **74**, 601.
- Bina, M.M. & Henry, B., 1990. Magnetic properties, opaque mineralogy and magnetic anisotropies of serpentinized peridotites from ODP Hole 670A near the Mid-Atlantic Ridge, *Phys. Earth planet. Inter.*, **65**, 88–103.
- Bleil, U. & Petersen, N., 1983. Variation in magnetization intensity and low temperature titanomagnetite oxidation of oceanic floor basalts, *Nature*, **301**, 384–388.
- Canales, J.P., Detrick, R.S., Lin, J. & Collins, J.A., 2000. Crustal and upper mantle seismic structure beneath the rift mountains and across a non-transform offset at the Mid-Atlantic Ridge, *J. geophys. Res.*, **105**, 2699–2719.
- Cannat, M., 1993. Emplacement of mantle rocks in the seafloor at mid-ocean ridges, *J. geophys. Res.*, **98**, 4163–4172.
- Cannat, M. *et al.*, 1995. Thin crust, ultramafic rocks exposures, and rugged faulting pattern at the Mid-Atlantic Ridge (22°–24°N), *Geology*, **23**, 49–52.
- Chen, W.P. & Molnar, P., 1983. Focal depths of intracontinental and intraplate earthquakes and their implications for the thermal and mechanical properties of the lithosphere, *J. geophys. Res.*, **88**, 4183–4214.
- Christensen, N.I., 1966. Elasticity of ultrabasic rocks, *J. geophys. Res.*, **71**, 5921–5931.
- Crane, K. & Ballard, R.D., 1981. Volcanics and structure of the FAMOUS narrowgate rift: evidence for cyclic evolution: AMAR 1, *J. geophys. Res.*, **86**, 5112–5124.
- Detrick, R.S., Needham, H.D. & Renard, V., 1995. Gravity anomalies and crustal thickness variations along the Mid-Atlantic Ridge between 33°N and 40°N, *J. geophys. Res.*, **100**, 3767–3787.
- Durand, C., Gente, P. & Dauteuil, O., 1995. Caractéristiques morphologiques des segments axiaux de la dorsale Médio-Atlantique entre 20°N et 24°N, *C. R. Acad. Sci.*, **320**, 411–418.
- Dyment, J., 1993. Evolution of the Indian Ocean Triple Junction between 65 and 49 Ma (Anomalies 28 to 21), *J. geophys. Res.*, **98**, 13 863–13 877.
- Dyment, J., 1998. Evolution of the Carlsberg Ridge between 60 and 45 Ma: ridge propagation, spreading asymmetry, and the Deccan-Reunion hotspot, *J. geophys. Res.*, **103**, 24 067–24 084.
- Dyment, J. & Arkani-Hamed, J., 1995. Spreading-rate-dependent magnetization of the oceanic lithosphere inferred from the anomalous skewness of marine magnetic anomalies, *Geophys. J. Int.*, **121**, 789–804.
- Dyment, J., Arkani-Hamed, J. & Ghods, A., 1997. Contribution of serpentinized ultramafics to marine magnetic anomalies at slow and intermediate spreading centres: insights from the shape of the anomalies, *Geophys. J. Int.*, **129**, 691–701.
- Gac, S., Dyment, J., Tisseau, C. & Goslin, J., 2003. Axial magnetic anomalies over slow-spreading ridge segments: insights from numerical 3-D thermal and physical modelling, *Geophys. J. Int.*, **154**(3), 618–632.
- Gente, P. *et al.*, 1994. Structures obliques sur les flancs de la dorsale Médio-Atlantique: traces fossiles de la propagation le long de l'axe de segments d'accrétion, *C. R. Acad. Sci.*, **318**, 1239–1246.
- Gente, P. *et al.*, 1995. Characteristics and evolution of the segmentation of the Mid-Atlantic Ridge between 20°N and 24°N during the last 10 million years, *Earth planet. Sci. Lett.*, **129**, 55–71.
- Hey, R., 1977. A new class of 'pseudofaults' and their bearing on plate tectonics: a propagating rift model, *Earth planet. Sci. Lett.*, **37**, 321–325.
- Hey, R., Duennebieber, F.K. & Morgan, W.J., 1980. Propagating rifts on mid-ocean ridges, *J. geophys. Res.*, **85**, 3647–3658.
- Hooft, E.E.E., Detrick, R.S., Toomey, D.R., Collins, J.A. & Lin, J., 2000. Crustal thickness and structure along three contrasting spreading segments of the Mid-Atlantic Ridge, 33.5°–35°N, *J. geophys. Res.*, **105**, 8205–8226.
- Irving, E., 1970. The Mid-Atlantic Ridge at 45°N, XIV, oxidation and magnetic properties of basalts: review and discussion, *Can. J. Earth Sci.*, **7**, 1528–1538.
- Juteau, T., Cannat, M. & Lagabrielle, Y., 1990. Serpentinized peridotites in the upper oceanic crust away from transform zones: a comparison of the results of previous DSDP and ODP legs, *Proc. Ocean Drill. Program Sci. Results*, **106–109**, 303–308.
- Kent, D.V., Honnorez, B.M., Opdyke, N.D. & Fox, P.J., 1978. Magnetic properties of dredged oceanic gabbros and the source of marine magnetic anomalies, *Geophys. J. R. astr. Soc.*, **55**, 513–537.
- Kong, L.S.L., Solomon, S.C. & Purdy, G.M., 1992. Microearthquake characteristics of a Mid-Ocean Ridge along-axis high, *J. geophys. Res.*, **97**, 1659–1685.
- Kuo, B.Y. & Forsyth, D.W., 1988. Gravity Anomaly of the Ridge Transform System in the South Atlantic between 31 and 34.5°S: upwelling centers and variation in crustal thickness, *Mar. geophys. Res.*, **10**, 205–232.
- Le Douaran, S. & Francheteau, J., 1981. Axial depth anomalies from 10 to 50° North along the Mid-Atlantic Ridge: correlation with other mantle properties, *Earth planet. Sci. Lett.*, **54**, 29–47.
- Lin, J., Purdy, G.M., Schouten, H., Sempéré, J.C. & Zervas, C., 1990. Evidence from gravity data for focused magmatic accretion along the Mid-Atlantic Ridge, *Nature*, **344**, 627–632.
- Lonsdale, P., 1994. Geomorphology and structural segmentation of the crest of the southern (Pacific-Antarctic) East Pacific Rise, *J. geophys. Res.*, **99**, 4683–4702.
- Macdonald, K.C., Sempéré, J.C. & Fox, P.J., 1984. East Pacific Rise from Siquieros to Orozco Fractures Zones: along-strike continuity of axial neovolcanic zone and structure and evolution of overlapping spreading centers, *J. geophys. Res.*, **3**, 211–215.
- Macdonald, K.C., Sempéré, J.C. & Fox, P.J., 1986. Reply: the debate concerning overlapping spreading centers and mid-ocean ridge processes, *J. geophys. Res.*, **91**, 10 501–10 511.
- Maia, M. & Gente, P., 1998. Three-dimensional gravity and bathymetry analysis of the Mid-Atlantic Ridge between 20°N and 24°N: flow geometry and temporal evolution of the segmentation, *J. geophys. Res.*, **103**, 951–974.
- Marshall, M. & Cox, A., 1972. Magnetic changes in pillow basalt due to sea-floor weathering, *J. geophys. Res.*, **77**, 6459–6469.
- Pariso, J.E. & Johnson, H.P., 1993. Do lower crustal rocks record reversals of the Earth's magnetic field? Magnetic petrology of oceanic gabbros

- from Ocean Drilling Program Hole 735B, *J. geophys. Res.*, **98**, 16 013–16 032.
- Phipps Morgan, J. & Sandwell, D.T., 1994. Systematics of ridge propagation south of 30°S, *Earth planet. Sci. Lett.*, **121**, 245–258.
- Ravilly, M., Dyment, J., Gente, P. & Thibaud, R., 1998. Axial magnetic anomaly amplitude along the Mid-Atlantic Ridge between 20°N and 40°N, *J. geophys. Res.*, **103**, 24 201–24 221.
- Ravilly, M., 1999. Etude de l'anomalie magnétique axiale le long de la ride médio-atlantique : implications sur les processus de l'accrétion et les variations temporelles du champ géomagnétique. *Thèse de doctorat*, Université de Bretagne Occidentale, Brest.
- Sempéré, J.C., Purdy, G.M. & Schouten, H., 1990. Segmentation of the Mid-Atlantic Ridge between 24°N and 30°40'N, *Nature*, **344**, 427–431.
- Sempéré, J.C., Lin, J., Brown, H.S., Schouten, H. & Purdy, G.M., 1993. Segmentation and morphotectonic variations along a slow-spreading center: the Mid-Atlantic Ridge (24°00'N–30°40'N), *Mar. geophys. Res.*, **15**, 153–200.
- Thibaud, R., Gente, P. & Maia, M., 1998. A systematic analysis of the Mid-Atlantic Ridge morphology and gravity between 15°N and 40°N: constraints of the thermal structure, *J. geophys. Res.*, **103**, 24 223–24 243.
- Tisseau, C. & Tonnerre, T., 1995. Non steady-state thermal model of spreading ridges: implication for melt generation and mantle outcrops, in *Mantle and Lower Crust Exposed in Ridges and Ophiolites*, pp. 181–214, eds Vissers, R.L.M. & Nicolas, A., Kluwer Academic Publishers, Netherlands.
- Tolstoy, M., Harding, A.J. & Orcutt, J.A., 1993. Crustal thickness on the Mid-Atlantic Ridge: bull's eye gravity anomalies and focused accretion, *Science*, **262**, 726–729.
- Toomey, D.R., Solomon, S.C., Purdy, G.M. & Murray, M.H., 1985. Microearthquakes beneath the median valley of the Mid-Atlantic Ridge near 23°N: hypocenters and focal mechanisms, *J. geophys. Res.*, **90**, 5443–5458.
- Toomey, D.R., Solomon, S.C. & Purdy, G.M., 1988. Microearthquakes beneath the median valley of the Mid-Atlantic Ridge near 23°N: tomography and tectonics, *J. geophys. Res.*, **93**, 9093–9112.
- Toomey, D.R., Purdy, G.M., Barclay, A.H., Wolfe, C.J. & Solomon, S.C., 1993. FARA microearthquakes experiments IV: implications of Mid-Atlantic Ridge seismicity for models of young oceanic lithosphere, *AGU Fall meeting*, **74**, 601.
- Wilson, D.S., Hey, R.N. & Nishimura, C., 1984. Propagation as a mechanism of reorientation of the Juan de Fuca ridge, *J. geophys. Res.*, **89**, 9215–9225.
- Weiland, C.M., Macdonald, K.C. & Grindlay, N.R., 1996. Ridge segmentation and the magnetic structure of the southern Mid-Atlantic Ridge 26°S and 31°–35°S: implications for magmatic processes at slow spreading centers, *J. geophys. Res.*, **101**, 8055–8073.
- Wolfe, C.J., Purdy, G.M., Toomey, D.R. & Solomon, S.C., 1995. Microearthquake characteristics and crustal velocity structure at 29°N on the MAR: the architecture of a slow spreading ridge, *J. geophys. Res.*, **100**, 24 449–24 472.